npg

Original Article

Phenylphthalazines as small-molecule inhibitors of urea transporter UT-B and their binding model

Jian-hua RAN[1, 2, #], Min LI[1, #], Weng-leong TOU[3, #], Tian-luo LEI[1], Hong ZHOU[1], Calvin Yu-Chian CHEN[4, 5, 6, *], Bao-xue YANG[1, *]

[1]Department of Pharmacology, School of Basic Medical Sciences, Peking University, and State Key Laboratory of Natural and Biomimetic Drugs, Beijing 100191, China; [2]Department of Anatomy, Laboratory of Stem and Tissue Engineering, Basic Medical College, Chongqing Medical University, Chongqing 400016, China; [3]School of Medicine, College of Medicine, China Medical University Hospital, Taichung 40402, Taiwan, China; [4]Human Genetic Center, Department of Medical Research, China Medical University Hospital, Taichung 40402, Taiwan, China; [5]Research Center for Chinese Medicine & Acupuncture, China Medical University, Taichung 40402, Taiwan, China; [6]Department of Biomedical Informatics, Asia University, Taichung 41354, Taiwan, China

Aim: Urea transporters (UT) are a family of transmembrane proteins that specifically transport urea. UT inhibitors exert diuretic activity without affecting electrolyte balance. The purpose of this study was to discover novel UT inhibitors and determine the inhibition mechanism.

Methods: The primary screening urea transporter B (UT-B) inhibitory activity was conducted in a collection of 10 000 diverse small molecules using mouse erythrocyte lysis assay. After discovering a hit with a core structure of 1-phenylamino-4-phenylphthalazin, the UT-B inhibitory activity of 160 analogs were examined with a stopped-flow light scattering assay and their structure-activity relationship (SAR) was analyzed. The inhibition mechanism was further investigated using *in silico* assays.

Results: A phenylphthalazine compound PU_{1424} , chemically named 5-(4-((4-methoxyphenyl) amino) phthalazin-1-yl)-2-methylbenzene sulfonamide, showed potent UT-B inhibition activity, inhibited human and mouse UT-B-mediated urea transport with IC_{50} value of 0.02 and 0.69 μmol/L, respectively, and exerted 100% UT-B inhibition at higher concentrations. The compound PU_{1424} did not affect membrane urea transport in mouse erythrocytes lacking UT-B. Structure-activity analysis revealed that the analogs with methoxyl group at R4 and sulfonic amide at R2 position exhibited the highest potency inhibition activity on UT-B. Furthermore, *in silico* assays validated that the R4 and R2 positions of the analogs bound to the UT-B binding pocket and exerted inhibition activity on UT-B.

Conclusion: The compound PU1424 is a novel inhibitor of both human and mouse UT-B with IC_{50} at submicromolar ranges. Its binding site is located at the So site of the UT-B structure.

Keywords: urea transport; UT-B; small-molecule inhibitor; phenylphthalazines; drug discovery; stopped-flow light scattering; *in silico*

Introduction

Urea is generated by the liver as the major end product of nitrogen metabolism; it is released into the blood and excreted by the kidneys. The processing of urea in the kidney is complex, involving countercurrent multiplication and exchange mechanisms that greatly increase urea concentrations in the renal medulla[1]. The renal countercurrent mechanisms involve intrarenal urea recycling through urea transporters (UT) expressed in renal tubule epithelial cells (UT-A isoforms)

and renal vasa recta microvessels (UT-B)[2, 3]. Functional and structural analysis showed that UT-A is a transmembrane channel protein that is selectively permeable to urea, and UT-B is permeable to urea, urea analogs and water[4–8]. Phenotype analysis of knockout mice lacking UT-B[9, 10] or various UT-A isoforms[11, 12] has provided evidence for the involvement of UT in the urinary concentrating mechanism.

The defective urinary concentrating function found in UT-knockout mice suggests the potential utility of UT inhibitors as 'urearetics' that would disrupt urinary concentrating function[2, 13]. Our previous work found a novel class of thienoquinolin UT inhibitors[14, 15]. The thienoquinolin UT inhibitors inhibited both UT-B- and UT-A-type urea transporters. Subcutaneous delivery of thienoquinolin to rats caused an increase in urine output, a decrease in the urine urea

concentration and subsequent osmolality without electrolyte disturbances or liver or renal damage, which suggests that the UT inhibitors have a diuretic effect by urea-selective diuresis. However, the maximum activity of thienoquinolin on mouse UT-B-mediated urea transport was only approximately 50%, which is too weak to establish a 'chemical knockout' mouse model.

Using an erythrocyte lysis assay as a high-throughput screening method, several classes of small-molecule UT inhibitors have been identified with submicromolar to micromolar $IC_{50}s^{[14, 16-20]}$. However, the most potent inhibitors identified against human UT-B were substantially less potent against mouse UTs, precluding proof-of-concept studies of their ureaaretic efficacy in mouse models of fluid retention and uremia.

Here, we report the screening of a collection of diverse compounds to identify potent inhibitors of mouse UT-B. Screening of 10 000 compounds and follow-up optimization by testing the structural analogs of the active compounds yielded a new UT inhibitor, PU_{1424}, with potent UT-B inhibition activity at submicromolar IC_{50} and 100% efficacy on human and mouse UT-B. PU_{1424} reversibly inhibited mouse UT-B. Structureactivity analysis suggested that the R2 and R4 positions of the compounds may participate in the inhibition mechanism. Furthermore, we validated that the R2 group or the R4 group was bound inside the So region of the UT-B through structurebased drug design, ligand-based and 3D-QSAR models.

Materials and methods
Chemical compounds
The primary screening was performed using a collection of 10 000 diverse, drug-like compounds from ChemDiv, Inc (San Diego, CA, USA), and 96-well plates containing a single compound per well (2.5 mmol/L) were prepared for screening and stored frozen in DMSO.

Collection of mouse and human blood
Venous blood was collected from 10–12 week-old (25–30 g) wild-type, AQP1-null or UT-B-null mice by orbital puncture following subcutaneous injection with sodium heparin (150 USP units). Human venous blood was collected into heparinized tubes, kept at 4 °C, and used within 48 h after collection. The protocols were approved by the ethics committee of Peking University.

Screening procedure
At the time of the assay, whole blood from wild-type mice was diluted to a hematocrit of 1% in hyperosmolar PBS containing 1.25 mol/L acetamide and 5 mmol/L glucose (1550 mOsm). Erythrocyte suspensions were maintained at room temperature for up to 2 h by periodic pipette mixing. Ninety-nine microliters from a reservoir containing the erythrocyte suspension were added to each well of a 96-well round-bottom microplate to which test compounds were added (1 µL, 25 µmol/L final compound concentration, 1% final DMSO concentration). After 6 min of incubation, 20 µL of the erythrocyte suspension were added rapidly to each well of a 96-well black-walled

plate (Costar, Corning, NY, USA) containing 180 µL isosmolar buffer (PBS containing 1% DMSO) in each well. Vigorous mixing was achieved by repeated pipetting. Erythrocyte lysis was quantified by measurement of the absorbance at 710 nm wavelength completed within 5 min after the hypoosmolar shock. Each assay plate contained eight negative 'no-lysis' controls (isotonic buffer; PBS+1.25 mol/L acetamide with 1% DMSO) and eight positive 'full-lysis' controls (distilled H_2O with 1% DMSO) that were mixed with DMSO vehicle-treated blood. The percentage of erythrocyte lysis in each test well of a given plate was calculated using control values from the same plate as $\%lysis=100\%\cdot(A_{neg}-A_{test})/(A_{neg}-A_{pos})$, where A_{test} is the absorbance value from a test well. A_{neg} and A_{pos} were negative control and positive control wells, respectively. Chemicals were purchased from Sigma-Aldrich (St Louis, MO, USA) unless otherwise noted.

Stopped-flow light scattering
Mouse or human erythrocyte urea permeability was measured by stopped-flow light scattering using an SX20 instrument (Applied Photophysics, Surrey, UK) as described previously[14]. For measurement of urea permeability, dilutions of mouse or human blood in PBS (hematocrit ~0.5%) were incubated with test compounds for 10 min and then subjected to a 250 mmol/L inwardly directed gradient of urea. After an initial osmotic shrinking phase, the kinetics of increasing cell volume caused by the urea influx was measured as the time-course of 90° scattered light intensity at 530 nm, with increasing cell volume producing reduced scattered light intensity. In some experiments, to assay reversibility, compounds were added to erythrocytes for 10 min and then washed with PBS three times by centrifugation for 1 h prior to stopped-flow measurements.

For the measurement of osmotic water permeability, suspensions of erythrocytes (0.5% hematocrit) in PBS were subjected to a 250 mmol/L inwardly directed gradient of sucrose. The kinetics of decreasing cell volume were measured from the time course of 90° scattered light intensity at 530 nm wavelength. Osmotic water permeability coefficients (P_f) were computed from the light scattering time course[5].

Structure-activity relationship
Approximately 160 commercially available analogs (ChemDiv Inc, San Diego, CA, USA) of active compounds identified in the primary screening were tested against human and mouse UT-B using the erythrocyte lysis assay. Doseresponse experiments were performed for some compounds (with human and/or mouse blood) by the lysis assay. EC_{50} was calculated by non-linear regression using the equation $\%lysis=\%lysis_{min}+(\%lysis_{max}\cdot[inh]^H)/(EC_{50}{}^H+[inh]^H)$, where $[inh]$ is the inhibitor concentration and H is the Hill coefficient.

Homology modeling and structure-based drug design
The Bos taurus (Bovine) UT-B protein rigid structure was downloaded from the Protein Data Bank (PDB: 4EZD) and used as a template to generate a mouse UT-B homology model[21]. The protein sequence of mouse UT-B was downloaded from Swis-

sprot (entry: Q8VHL0)[22]. Sequence alignment was performed by a multiple alignment scoring matrix, BLOcks SUbstitution Matrix (BLOSUM), with a 10 gap open penalty[23]. Predicted structures were then evaluated for validity by RAMPAGE[24, 25]. The urea binding site (Sm, So) and urea were conserved in the predicted mouse UT-B. The clustering of the binding pose of the ligand via structure-based drug design is necessary for evaluating functional group-residue interaction details. Force field Chemistry at HARvard Macromolecular Mechanics (CHARMm) was employed to start minimization after Monte Carlo docking simulation was performed. Docking pose minimization and clustering with 1.5 (RMS threshold for diversity) was generated by a receptor-rigid docking algorithm (Ligand-Fit) to calculate binding affinity[26].

3D-QSAR and ligand-based drug design

Two-hundred descriptors of chemical properties were produced by Discovery Studio 2.5 before genetic function approximation (GFA) calculation[27]. Those descriptors with higher correlation were sorted on a square correlation coefficient (R^2) through GFA. The representative descriptors associated with bioactivity were used in the randomization of the training sets and test sets. Bioactivity was predicted by Support Vector Machine (SVM)[28] and Multiple Linear Regression (MLR) to evaluate the fraction of properties. LibSVM and MAT-LAB R2010a (MathWorks Inc, Natick, MA, USA) were used to produce linear and non-linear models of SVM and MLR. Observed bioactivity was compared with the SVM/MLR predicted bioactivity to calculate the square correlation coefficient (R^2), with $R^2 > 0.5$ classified as confident. In this study, ligand-based drug design was used in complement of 3D-QSAR models[29, 30]. Comparative force field analysis (CoMFA) and comparative similarity indices analysis (CoMSIA) were used to study steric (S) and electrostatic (E) properties, hydrophobic (H) and hydrogen donor/acceptors (D/A). The atom-fit module of SYBYL-X 1.1 (Tripos, St Louis, MO, USA) was used to conduct scaffold alignment of the training set and the test set. S and E properties were calculated using Lennard-Jones potential and Coulombic potential in CoMFA, respectively. In CoMSIA, five properties including S/H/A/D/E were calculated from Gaussian functions. Finally, partial least squares (PLS) analysis was used to generate models and produce the conventional correlation coefficient (r^2) in the non-cross validation model and the cross-validated coefficient (q^2) in the cross validation model. The model with the lowest standard error of estimate and standard error and the highest q^2 and r^2 values was selected as the optimum model.

Results

Identification of small-molecule UT-B inhibitors

A collection of 10 000 small, drug-like compounds with high chemical diversity was screened at 25 μmol/L in the primary screen using the mouse and human erythrocyte lysis model[14]. One compound, chemically named 2-(4-((4-(4-methoxyphenyl) phthalazin-1-yl) amino) phenoxy) acetamide (Figure 1A) with a core structure of 1-phenylamino-4-phenylphthalazin (Figure

1B) showed an apparent UT-B inhibitory activity in mouse erythrocytes.

We screened 160 commercially available analogs of 1-phenylamino-4-phenylphthalazin to establish structure-activity relationship and to identify compounds with improved UT-B inhibitory potency. The structural characteristics and IC_{50} values for this class of compounds with inhibition activity are summarized in Table 1. All the selected compounds contained Me, OMe, $OCH_2C≡CH$ as R1 and an H group as R3. A methoxyl group at the R4 (PU_{1424}, PU_{1451}, PU_{1627}, PU_{1957}, PU_{5466}, PU_{2026}, PU_{1910}) enhanced the inhibitory activity compared with NHAc (acetamide), $OCH_2C(O)NHMe$ (2-hydroxy-*N*-methyl-acetamide), $C(O)NH_2$ (formamide), or $OCH_2C(O)NH_2$ (methyl carbamate) groups (PU_{2413}, PU_{2011}, PU_{2014} and PU_{2013}, PU_{2018}, PU_{5765}, PU_{2027}, PU_{1990} and PU_{2020}). Furthermore, inhibitory activity was reduced with an SO_2NH_2 (sulfonic amide) group at the R2 position (PU_{1424}) as a substitute for SO_2NHMe, 1-methyl-4-(sulfonyl) piperazine, SO_2NMe_2, *N*-(pyridin-2-ylmethyl) sulfonamide, $SO_2NH(CH_2)_2OH$, SO_2NEt_2, sulfonylmorpholine, sulfonylpiperidine, *N*-[(1H-benzo[d]imidazol-2-yl)methyl]imidazol] sulfonamide, or *N*-(1-hydroxy-2-methylpropan-2-yl)sulfonamide (PU_{1451}, PU_{2112}, PU_{1627}, PU_{1957}, PU_{5466}, PU_{1935}, PU_{2026}, PU_{1910}, PU_{1980}, PU_{2138}, PU_{2347}). Structure-activity relationship analysis indicated that a methoxyl group at R4 and a sulfonic amide at the R2 position of the compounds may play an important role in the UT-B inhibition mechanism.

The best compound was PU_{1424}, chemically named 5-(4-((4-methoxyphenyl) amino) phthalazin-1-yl)-2-methyl-benzenesulfonamide (Figure 1C), with an IC_{50} of 1.61 μmol/L in the mouse model (Figure 1D), as determined by erythrocyte lysis assay. The maximal inhibition rate (I_{max}) of PU_{1424} on acetamide transport mediated mouse erythrocyte lysis was more than 80%. PU_{1424} did not change the lysis rate of UT-B null mouse erythrocytes, which indicated that PU_{1424} did not affect non-UT-B-mediated transmembrane urea transport. PU_{1424} caused the same erythrocyte lysis rates in wild-type mice as in UT-B null mice, which suggested that PU_{1424} inhibited 100% of UT-B activity. The I_{max} values from the erythrocyte lysis assay were not absolute inhibition rates of urea transport because of nonlinearity between acetamide permeability and the percentage erythrocyte lysis rate, in addition to some extent of acetamide simple diffusion across the lipid bilayer of the cell membrane[6].

UT-B inhibition mechanism

To determine the inhibition efficacy of PU_{1424} on mouse UT-B, mouse erythrocytes were assayed by a stopped-flow light scattering from the kinetics of urea influx (erythrocyte swelling) in response to an inwardly directed urea gradient. Rapid mixing of an erythrocyte suspension with a hyperosmolar solution containing an excess of 250 mmol/L urea produced rapid cell shrinking due to osmotic water efflux, followed by cell swelling as urea (and water) influx occurred. PU_{1424} significantly inhibited UT-B-facilitated urea transport in the dose response shown in Figure 1E. The IC_{50} of PU_{1424} on mouse erythrocytes deduced from stopped-flow measurement was 0.69 μmol/L

Table 1. Structure-activity analysis of phenylphthalazines.

Compound	R1	R2	R3	R4	IC$_{50}$ (µmol/L)
5754-2826	OCH$_2$C≡CH	H	H	NHAc	6.463±0.256
4109-2007	OMe	H	H	OCH$_2$C(O)NH$_2$	4.149±0.407
8012-5765	Me	*N*-(pyridin-2-ylmethyl)sulfonamide	H	OCH$_2$C(O)NH$_2$	9.692±0.376
4109-2010	Me	SO$_2$NH$_2$	H	OCH$_2$C(O)NHMe	7.964±1.840
4109-2011	Me	SO$_2$NHMe	H	OCH$_2$C(O)NHMe	5.991±0.227
4109-2014	Me	SO$_2$NMe$_2$	H	OCH$_2$C(O)NHMe	3.453±0.103
4109-2013	Me	SO$_2$NMe$_2$	H	OCH$_2$C(O)NH$_2$	6.796±0.357
4109-2026	Me	SO$_2$NEt$_2$	H	OCH$_2$C(O)NHMe	7.141±0.375
4109-2416	Me	SO$_2$NiPr	H	OCH$_2$C(O)NHMe	7.024±1.020
4109-2018	Me	SO$_2$NtBu	H	OCH$_2$C(O)NHMe	3.955±0.766
4109-2020	Me	Sulfonylmorpholine	H	OCH$_2$C(O)NHMe	6.338±0.372
5233-2390	Me	*N*-(1-hydroxy-2-methylpropan-2-yl)sulfonamide	H	OCH$_2$C(O)NHMe	3.113±0.121
5233-2329	Me	*N*-[(tetrahydrofuran-2-yl)methyl]sulfonamide	H	OCH$_2$C(O)NMe	6.081±0.345
5233-2413	Me	SO$_2$NH$_2$	H	NHAc	1.913±0.291
3635-1424	Me	SO$_2$NH$_2$	H	OMe	1.613±0.192
3635-1451	Me	SO$_2$NHMe	H	OMe	1.992±0.250
3938-1627	Me	SO$_2$NMe$_2$	H	OMe	2.916±0.914
4109-2026	Me	SO$_2$NEt$_2$	H	OMe	3.934±0.196
4109-1957	Me	SO$_2$NHtBu	H	OMe	3.033±0.096
4109-2029	Me	SO$_2$NHCH$_2$CO$_2$Et	H	OMe	1.833±0.234
4109-1980	Me	Sulfonylpiperidine	H	OMe	5.437±2.301
4109-1910	Me	Sulfonylmorpholine	H	OMe	4.180±0.646
4109-1990	Me	Sulfonylmorpholine	H	C(O)NH$_2$	6.101±0.230
4109-1935	Me	SO$_2$NH(CH$_2$)$_2$OH	H	OMe	3.614±1.591
4903-2112	Me	1-Methyl-4-(sulfonyl)piperazine	H	OMe	2.761±0.442
4903-2138	Me	*N*-[(1H-benzo[d]imidazol-2-yl)methyl]sulfonamide	H	OMe	6.793±4.237
5233-2347	Me	*N*-(1-hydroxy-2-methylpropan-2-yl)sulfonamide	H	OMe	8.331±0.341
8012-5466	Me	*N*-(pyridin-2-ylmethyl)sulfonamide	H	OMe	3.316±0.117

(Figure 1F). The I_{max} of PU$_{1424}$ at 10 µmol/L on UT-B mediated urea transport was nearly 100%. The IC$_{50}$ of PU$_{1424}$ on human erythrocytes deduced from stopped-flow measurement was approximately 0.02 µmol/L. The I_{max} of PU$_{1424}$ at 2.5 µmol/L on UT-B mediated urea transport was close to 100% (Figure 1G).

The inhibition activity of PU$_{1424}$ was low when stopped-flow light scattering was performed by exposing erythrocytes to PU$_{1424}$ at 4 µmol/L for 10 min followed by washout with PBS for 1 h (Figure 2A, 2B), which suggested that the inhibition activity of PU$_{1424}$ was partially reversible.

Inhibition of UT-B-facilitated water transport in erythrocytes

PU$_{1424}$ was used to assess the contribution of UT-B to osmotic water permeability in mouse erythrocytes. Osmotic water permeability (P$_f$) was measured by stopped-flow light scattering in erythrocytes from wild-type and AQP1-null mice. There was no significant change in the P$_f$ in PU$_{1424}$ treated wild-type erythrocytes in which AQP1 mediated approximately 90% of P$_f$.[5] PU$_{1424}$ significantly reduced P$_f$ from 0.0018±0.0002 cm/s to 0.0004±0.0001 cm/s in AQP1-null erythrocytes (Figure 2C).

Structure-based drug design

The docking results showed that UT-B inhibitors bound to UT-B in two different ways: in the first binding method,

the R2 group was bound inside the So region; in the second binding method, the R4 group was bound inside the So region. Regardless of the binding methods, the core structures were incorporated completely into the binding pockets formed by L280, W281, A315 or Y316 (Figure 3). With respect to the 25 other analogs tested during the cross-species *in silico* studies under the volume restricted binding site conditions, compounds PU$_{2026}$, PU$_{2018}$, and PU$_{2329}$ did not bind to the human UT-B, whereas PU$_{1424}$ displayed the best mouse UT-B binding capacity (see Figure 4). Moreover, various binding patterns for PU$_{2026}$, PU$_{2018}$, PU$_{2329}$ and PU$_{1424}$ were observed in the mouse model. Specifically, PU$_{2026}$, PU$_{2329}$ and PU$_{1424}$ bound through the first method, whereas PU$_{2018}$ used the second method to bind in the mouse model. It is noteworthy that only PU$_{1424}$ could bind with the human UT-B using the second method. In contrast, PU$_{2026}$, PU$_{2018}$ and PU$_{2329}$ used the first method to bind to the volume unrestricted binding sites of the human UT-B. The hydrophilia of the R4 hydroxyl group of PU$_{2390}$ kept it away from the So region, and PU$_{2026}$, PU$_{2329}$ and PU$_{1424}$ combined with UT-B in the same way as PU$_{2390}$.

With respect to the functional groups present in PU$_{2026}$, PU$_{2416}$ and PU$_{2018}$, all of the compounds included the OCH$_2$C(O)NHMe group as the R4. However, among these three compounds, only PU$_{2416}$ combined with the cross-spe-
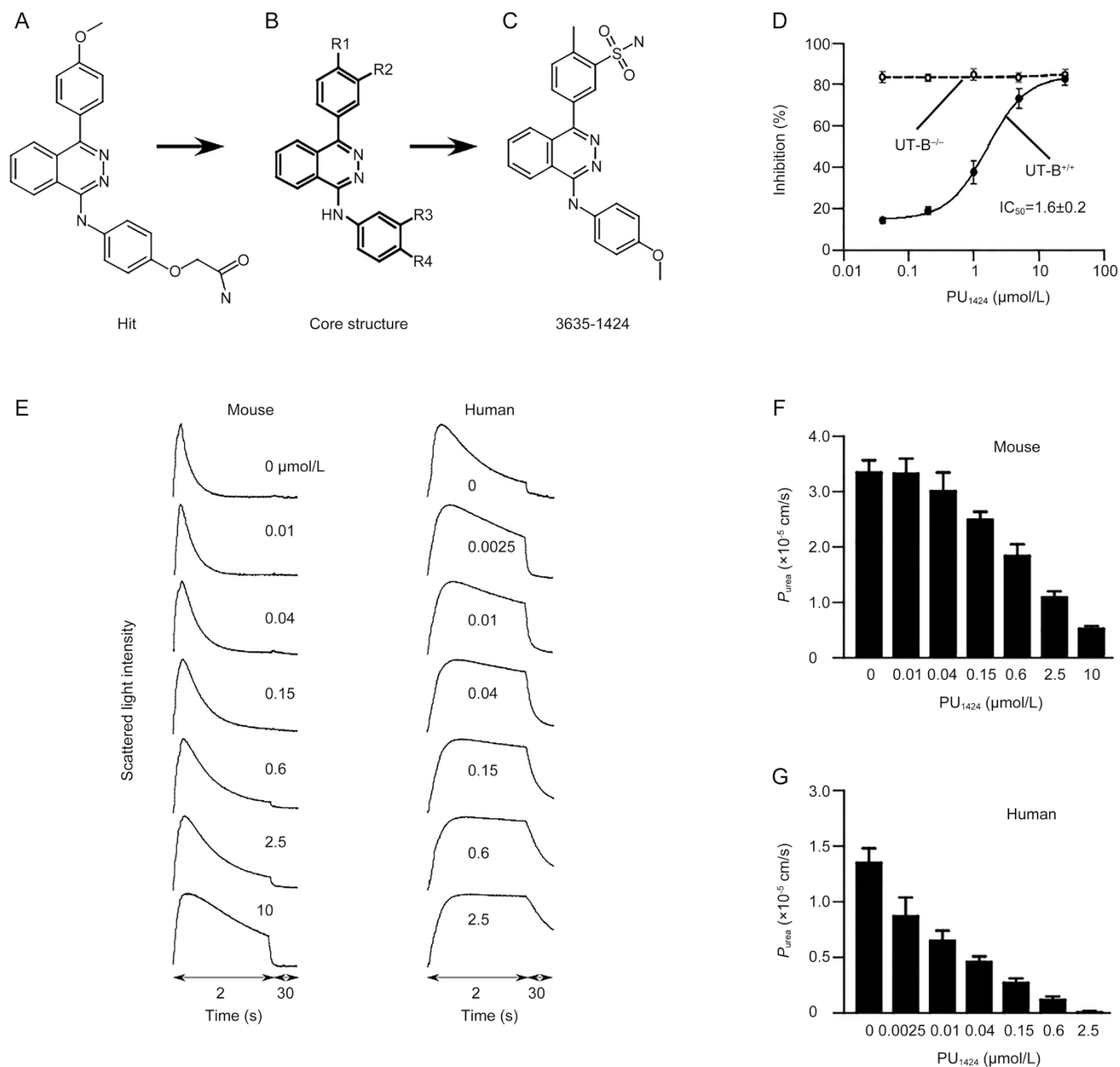
Figure 1. Activity of phenylphthalazines against UT-B in mouse model. (A) Chemical structure of hit. (B) Core structure of hit. (C) Chemical structure of PU_{1424}. (D) Urea permeability (P_{urea}) in mouse erythrocytes. Mean±SEM. $n=10$. (E) Concentration-inhibition curves for the time course of scattered light intensity measured in mouse erythrocytes (left) or human erythrocytes (right) in the absence (top) or presence of PU_{1424} at indicated concentration for 10 min at 10 °C in response to a 250 mmol/L inwardly directed urea gradient. (F) Dose-dependent inhibition activity for PU_{1424} in erythrocytes from wild-type mice. Mean±SEM. $n=3$. (G) Urea permeability (P_{urea}) in human erythrocytes. Mean±SEM. $n=10$.

cies UT-B because the R4 group in PU_{2416} is a straight chain, whereas those in PU_{2026} and PU_{2018} have branched structures. Furthermore, both PU_{2018} and PU_{2026} have a dimethylsulfoamoyl group in common. However, because of the steric properties, the SASA of PU_{2026} is lower than that of PU_{2026} (the lower the SASA, the easier it is for a compound to bind to a smaller size binding site). Actually, PU_{2026} is very similar to PU_{1424}. It should be noted that PU_{1424} had the lowest IC_{50} among all the 28 compounds and the lowest relative SASA. However,

PU_{1424} did not form any hydrogen bonds during the cross-species study. By contrast, the core structure of PU_{2018} and the *N*-[(tetrahydrofuran-2-yl)methyl]sulfonamide of PU_{2329} exhibited hydrogen bonding in the mouse UT-B D275 and the human UT-B D280, respectively.

3D-QSAR and Ligand-Based Drug Design
GFA model=–1371.7+0.097833*Molecular_SASA+277.97*CIC+1396.6*SIC–0.012377*V_DIST_equ–2.4916*CHI_0+
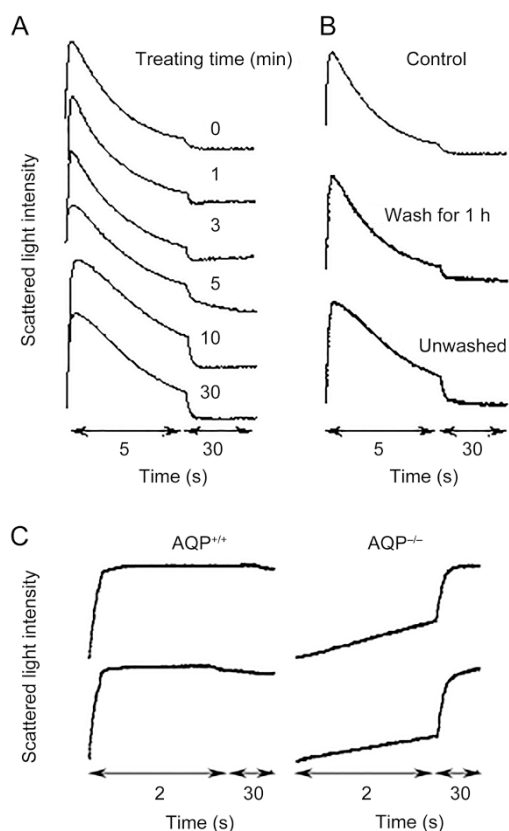
Figure 2. Characteristics of UT-B inhibition and water permeability in mouse erythrocytes. (A) Presentative stopped-flow light scattering curves of erythrocytes treated with 4 μmol/L PU1424 for different time (*n*=10). (B) Presentative stopped-flow light scattering curves for reversibility of UT-B inhibition. Prior to the stopped-flow measurements, 4 μmol/L PU1424 was washed out after 10 min-incubation (*n*=10). (C) Scattered light intensity measured in wild-type mouse erythrocytes (left) or AQP1 null erythrocytes (right) in the absence (top) or presence of 4 μmol/L PU_{1424} (bottom) for 10 min at 10 °C in response to a 250 mmol/L inwardly directed sucrose gradient (*n*=10).

$0.013998*Jurs\_DPSA\_2+0.16468*Minimized\_Energy-0.0034628*PMI\_Y+2.7894*Shadow\_nu-34.237* Shadow\_XYfrac$

The representative descriptors, viz (1) Molecular_SASA, (2) CIC, (3) SIC (4) V_DIST_equ, (5) CHI_0, (6) Jurs_DPSA_2, (7) Minimized_Energy, (8) PMI_Y, (9) Shadow_nu, and (10) Shadow_XYfrac (Table S1), were determined by GFA method, which generated a model with a coefficient of determination (R^2) of 0.941 and a *P*-value <0.005. The SVM and MLR models were also tested using the aforementioned descriptors to pre-evaluate the validity of the quantitative structure-activity relationship. Descriptors such as the molecular accessible surface area had contributed greatly to the determination of the bio-activity in UT-B, for instance, the SASA of PU_{2026}, PU_{2018}, PU_{2329} and PU_{1424} were 799.16, 787.904, 802.425 and 635.935, respectively. The SVM and MLR models were suitable for prediction (>0.8) with an R^2 of 0.8978 and 0.8269, respectively (Figure 5).

The PLS results generated by QSAR models have been listed

in Table 2. Moreover, the primary parameter of CoMFA was the steric property (S), whereas for CoMSIA, the primary parameters were steric, hydrophobic, electrostatic and hydrogen bond donor. The CoMFA models were generated with non-cross validation and cross validation correlation coefficients r^2 and q^2, of values 0.937 and 0.509, respectively, under an optimal number of components (ONC) of six. Similarly, the properties were coupled to construct the CoMSIA models with r^2 and q^2 values of 0.954 and 0.628, respectively, under an ONC of six. Additionally, the correlation coefficients (R^2) of the CoMFA and CoMSIA models were 0.9369 and 0.954, respectively, which represented a suitable bioactivity prediction (>0.6) (Figure 5).

The CoMSIA 3D contour map established by the PLS has produced six types of contours: the steric favored (green, Sf), the steric disfavored (magenta, Sd), the hydrophobic favored (orange, Hf), the hydrophobic disfavored (white, Hd), the hydrogen bond donor favored (cyan, HBDf) and the HBD disfavored (blue, HBDd) (Figure 6A). The 3D contours established by the CoMSIA are primarily concentrated in the two regions of R1, R2, and the R4 functional groups. Because R2 had the most variations amongst the numerous compounds, R2 formed the bulk that crossed the proximity of R1 and R2 from a variety of angles and directions during the scaffold alignments. The contours at close proximities to the substituents were different. Hf was on top of R1, and the bottom of R1 was surrounded by a variety of contours formed by R2 (Figure 6B, top view, circle b). The remote-end of R2 was surrounded by Sd, which was divided into three major regions (Figure 6B, side view, circle a). The side view observation shows the left, right, and the inferior regions. Hf and Sf were generated at the close-end, R3 was surrounded by HBDf, and R4 was surrounded by Sd (Figure 6B, front view, circle c). Not every R2 of the compound could participate in the formation of the left, right and inferior contour regions during the alignment. Only the compounds PU_{2329}, PU_{1627}, PU_{2026}, PU_{1957}, PU_{2029}, PU_{1935}, PU_{2138} and PU_{5466} participated in the inferior regions, and only compounds PU_{2329}, PU_{1935}, PU_{2138} and PU_{5466} could participate in the formation of the remote inferior regions. We observed the structure-activity relationship of PU_{1424}, which had the best IC_{50} among the PU_{2138} compounds, and the top view of the inferior region of the PU_{1424} R1 methyl group showed the Hd, HBDd, Hf and Sf contours. However, R1 did not fit or participate in the formation of any contour. The benzene rings connecting R1 and R2 were in the Sd counter, but they did not participate in the formation of the Sd counter. The R2 sulphonamide group did participate in the contour formation of the Sf and Hf. R3 did not participate in any contour formation, but the close-end region of R4 did participate in parts of the HBDf contour formation. The results indicated that the redesigned PU_{1424} must strengthen the steric and hydrophobic (lipophilic) properties of R2. The lower the molecular weight of R2 (the SASA will usually decline for the same reason), the more it can maintain the same hydrophobic properties at the same time and strengthen the bioactivity of PU_{1424} in UT-B.
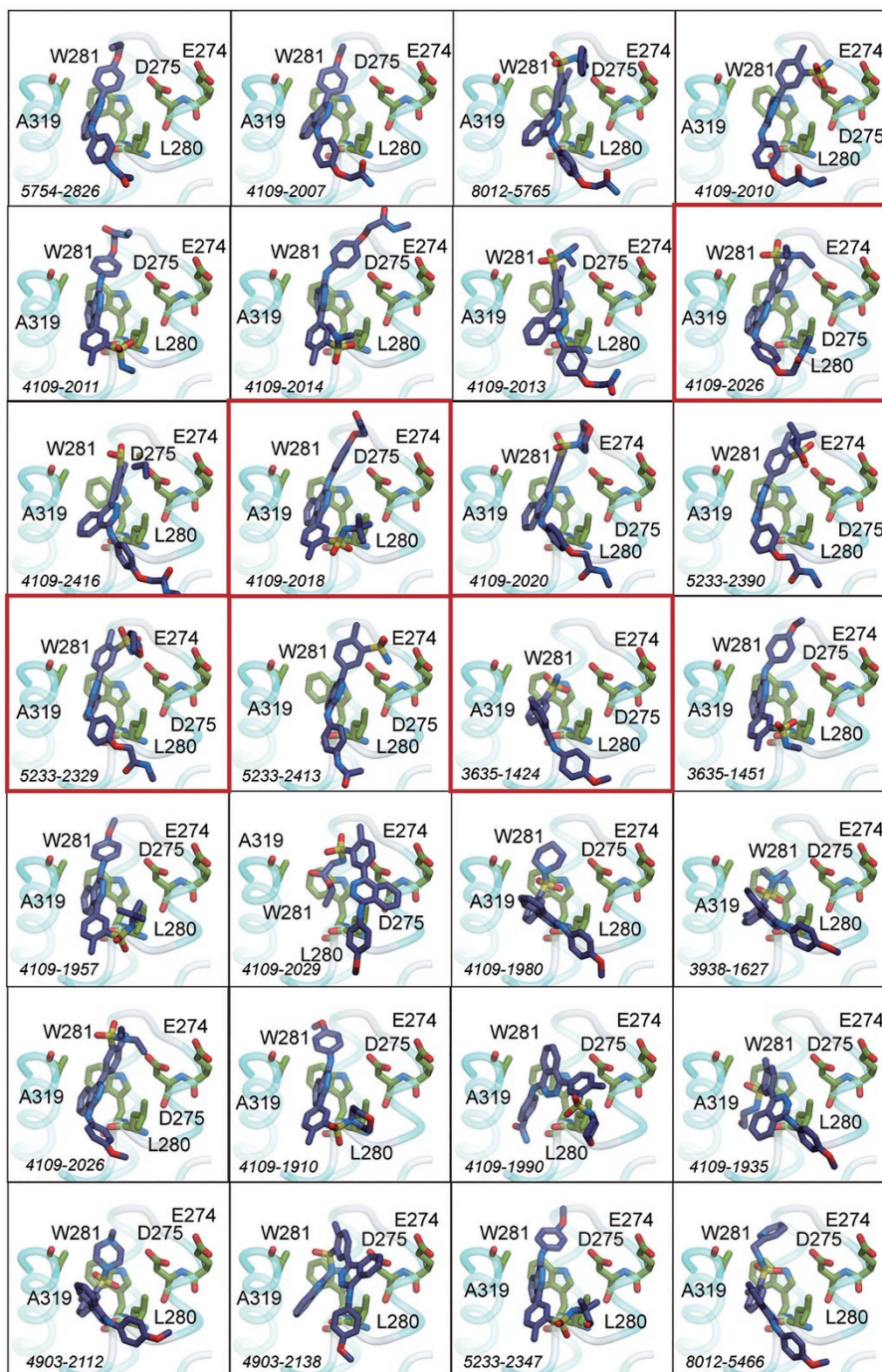
Figure 3. Docking pose of UT-B inhibitor in mouse UT-B. The red boxes illustrate PU_{2026}, PU_{2018}, PU_{2329} and PU_{1424}. The combination of displays illustrates the different substituents combining with UT-B using different methods where the R4 binding points of the PU_{2026}, PU_{2329} and PU_{1424} are in close proximity to the So region; however, PU_{2018} binds right at the So region using the R2 binding method.

Discussion

Urea transporters have been regarded as a diuretic target to develop novel diuretics[2, 31–33]. Several classes of UT-B inhibitors, including thienoquinolins, triazolothieno-pyrimidines, 2,7-disubstituted fluorenones, and DMTU have been identified by high throughput screening[14, 17–19, 34]. However, some unsatisfactory characteristics remain before

these active compounds can be developed into diuretics for clinical use or toll drugs for UT-B chemical knockout mouse model. It is therefore necessary to discover novel active small molecules with UT inhibition activity.

The present study discovered a potent small-molecule UT-B inhibitor, PU_{1424}, using an erythrocyte osmotic lysis assay. PU_{1424} exhibited inhibition activity on both human and mouse
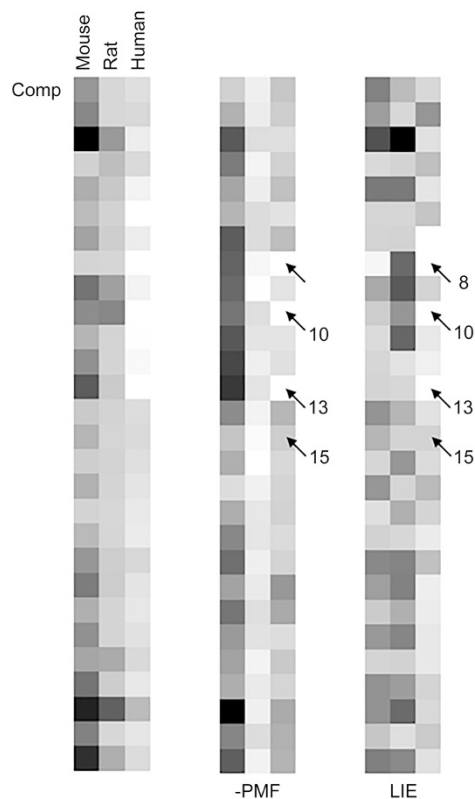
Figure 4. 3D-QSAR and ligand-based drug design. The heat map illustrates the binding affinity (left panel), potential of mean force (middle panel), and ligand internal energy (right panel) of the analogs on UT-B. The arrows show that PU_{2026}, PU_{2018} and PU_{2329} do not bind to the binding site of the volume restricted human UT-B.

UT-B. However, its inhibition activity was much stronger on human UT-B than on mouse UT-B. The structure-activity analysis of analogs revealed compounds with a wide range of potencies for the inhibition of UT-B. A methoxyl group at R4 and a sulfonic amide at the R2 position of compounds exhibited the highest potent inhibition activity on UT-B, which suggested that the R4 and R2 positions of the compounds may participate in the inhibition mechanisms.

UT-B is also permeable to water[4, 5]. Stopped-flow light scattering showed that PU_{1424} significantly inhibited mouse UT-B-mediated water permeability, which indicated that PU_{1424} blocked the water and urea common channel. Both the stopped-flow light scattering experiments and the *in silico* computational analysis suggested that PU_{1424} reversibly inhibited UT-B activity and PU_{1424} targeted the extracellular portion of the UT-B protein.

We have analyzed the binding site of UT-B inhibitors via an *in silico* assay and validated by 3D-QSAR and a cross-species study, which provided a structural basis for lead identification and optimization of UT-B inhibitors[35]. Using *in silico* assay, PU_{1424} was found to bind in two different ways: in the first binding method, the R2 group was bound inside the So region;

and in the second binding method, the R4 group was bound inside the So region. PU_{1424} bound to mouse UT-B using the first method, whereas it bound with the human UT-B using the second method. Quantitative structure-activity relationship (QSAR) models discovered that R2 formed the bulk that crossed the proximity of R1 and R2 from a variety of angles and directions during the scaffold alignments. The R2 sulphonamide group did participate in the contour formation of the Sf and Hf. R3 did not participate in any contour formation, but the close-end region of R4 did participate in parts of the HBDf contour formation, suggesting that PU_{1424} could strengthen its inhibition activity by decreasing the molecular weight of R2.

The urea penetration pathway can be subdivided in to So (outer), Sm (middle) and Si (inner) regions. Our previous data from the human UT-B model suggested that there is a binding pocket located primarily near the So site. Depending on the ligand structure and property, the binding pocket may influence the Sm directly by forming a steric bulk or indirectly by initiating the induced-fit mechanism. Our result in this manuscript suggested that the properties of PU_{1424} are less likely to initiate induced-fit mechanisms because it has failed to bind into the functional group docking (FGD) small pocket. CoMFA and CoMSIA studies revealed that the steric favor properties anchored near the So site and the distal region of the binding pocket. Moreover, the hydrophobic properties anchored near the distal region of the binding pocket. On the other hand, the structural similarity (91.3%) and identity (83.5%) between mouse and human models may play an important role in the binding affinity. In human UT-B, residues such as I206, N289, D280, W286, N328 and A337 were found to be important in the inhibitor-binding site near the So site. However, residues of the inhibitor-binding site include I206, V324 and N328 in humans, which are different from mice (I206→V201; V324→A319; N328→H323). Although there was an increased volume of the binding site due to the shortening of the side chain in V201 and A319, it did not increase the cluster number of the binding pose. The docking results suggested that histidine might interact in a face-to-face or offset-face stacked orientation with the surrounding residues. These interactions resulted in PU_{1424} binding toward the So region (5.359 Å from the original binding site; 7.092 Å to the So site). This might explain the significant bioactivity and steric mechanism of PU_{1424} compared to other analogs in mouse UT-B. Although the aforementioned *in silico* experiment provided the preliminary data, it provided a molecular level insight into the problem of the location of the inhibitor-binding pocket and the mechanism of inhibition.

In conclusion, the results of this study suggest that PU1424 inhibited UT-B-mediated transmembrane urea transport with a submicromolar IC_{50} level, and the inhibition activity was much stronger on human UT-B than on mouse UT-B. The R4 and R2 positions of the compounds were involved in the binding site at the extracellular portion of the UT-B protein, which provides a theoretical basis for further optimization of the chemical structure of UT inhibitors and screening a novel class of active compounds.

Table 2. The partial least squares analysis results generated by quantitative structure–activity relationship (QSAR) models.

	Cross validation		Non–cross validation			Fraction				
	ONC	q^2cv	r^2	SEE	F	S	E	H	D	A
CoMFA	6	0.509	0.937	0.655	34.631	1.000	0.000	–	–	–
CoMSIA										
S	6	0.691	0.663	1.513	4.588	1.000		–	–	–
E	6	NA	0.663	1.513	4.588	–	1.000		–	–
H	6	0.402	0.882	0.895	17.458	–	–	1.000		–
D	6	0.470	0.757	1.284	7.274	–	–	–	1.000	
A	6	0.233	0.803	1.156	9.510	–	–	–	–	1.000
SE	6	0.658	0.663	1.513	4.588	1.000	0.000	–	–	–
SH	6	0.766	0.867	0.948	15.275	0.313	–	0.687	–	–
SD	6	0.477	0.939	0.645	35.686	0.367	–	–	0.633	–
SA	6	0.370	0.890	0.863	18.938	0.312	–	–	–	0.688
EH	6	0.510	0.882	0.895	17.458	–	0.000	1.000	–	–
ED	6	0.339	0.757	1.284	7.274	–	0.000	–	1.000	–
EA	6	0.265	0.803	1.156	9.510	–	0.000	–	–	1.000
HD	6	0.486	0.940	0.638	36.581	–	–	0.474	0.526	–
HA	6	0.434	0.902	0.815	21.505	–	–	0.435	–	0.565
DA	6	0.426	0.814	1.123	10.221	–	–	–	0.493	0.507
SEH	6	0.814	0.867	0.948	15.275	0.313	0.000	0.687	–	–
SED	6	0.586	0.939	0.645	35.686	0.367	0.000	–	0.633	–
SEA	6	0.322	0.890	0.863	18.938	0.312	0.000	–	–	0.688
SHD	6	0.681	0.954	0.559	48.362	0.189	–	0.341	0.469	–
SHA	6	0.394	0.914	0.763	24.885	0.197	–	0.345	–	0.459
SDA	6	0.478	0.905	0.804	22.161	0.201	–	–	0.421	0.378
EHD	6	0.390	0.940	0.638	36.581	–	0.000	0.474	0.526	–
EHA	6	0.347	0.902	0.815	21.505	–	0.000	0.435	–	0.565
EDA	6	0.313	0.814	1.123	10.221	–	0.000	–	0.493	0.507
HDA	6	0.300	0.896	0.842	20.000	–	–	0.269	0.392	0.339
SEHD	6	0.628	0.954	0.559	48.362	0.189	0.000	0.341	0.469	–
SEHA	6	0.488	0.914	0.763	24.885	0.197	0.000	0.345	–	0.459
SEDA	6	0.464	0.905	0.804	22.161	0.201	0.000	–	0.421	0.378
SHDA	6	0.259	0.921	0.733	27.141	0.134	–	0.214	0.373	0.279
EHDA	6	0.313	0.896	0.896	20.000	–	0.000	0.269	0.392	0.339
SEHDA	6	0.407	0.921	0.733	27.141	0.134	0.000	0.214	0.373	0.279

Author contribution
Bao-xue YANG, Yu-Chian CHEN, Jian-hua RAN, Min LI, and Weng Ieong TOU participated in the study design and manuscript preparation; Jian-hua RAN, Min LI, and Weng Ieong TOU performed the experiments; Jian-hua RAN, Min LI, Weng Ieong TOU, Tian-luo LEI, Hong ZHOU, Yu-Chian CHEN and Bao-xue YANG analyzed the data. All authors read and approved the final version of the manuscript.

Supplementary information
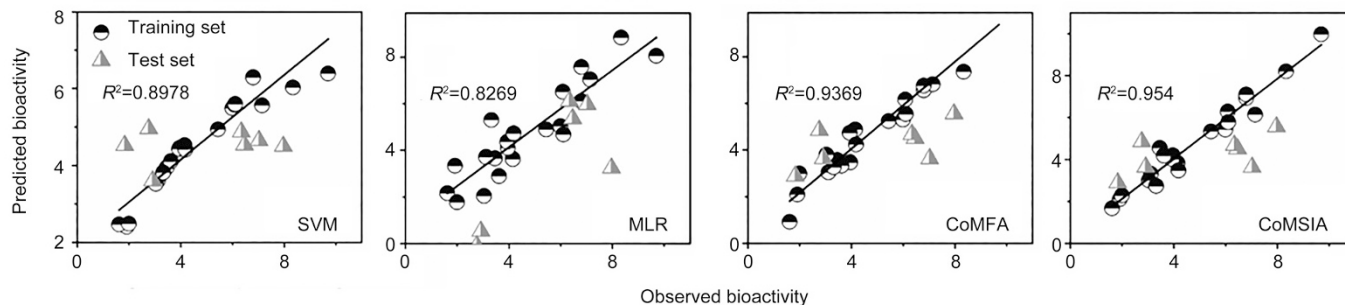Supplementary information is available at Acta Pharmacologica Sinica's website.

Figure 5. The correlation coefficients (R^2) of SVM, MLR, CoMFA and CoMSIA.
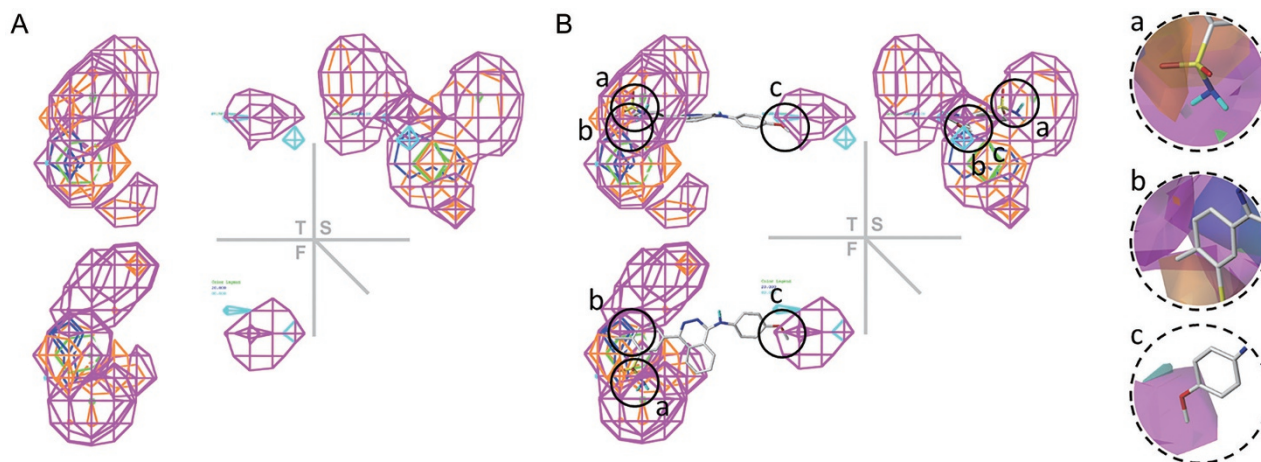

Figure 6. (A) Contour map in the presence of CoMSIA. (B) Relative position of the analog on the contour map after the scaffold alignment. Circles a/b/c represent R2/R1/R3, respectively. The side view (S) observation indicates that the R1/R2 contours are divided into three major regions: the left, the right, and the inferior contour regions. Different substituents were involved in the formation of the various contours. T, top view; F, front view.

References

1 Bankir LT, Trinh-Trang-Tan MM. Renal urea transporters. Direct and indirect regulation by vasopressin. Exp Physiol 2000; 85: 243S–252S.

2 Yang B, Bankir L. Urea and urine concentrating ability: new insights from studies in mice. Am J Physiol Renal Physiol 2005; 288: F881–96.

3 Fenton RA, Yang B. Urea transporter knockout mice and their renal phenotypes. Subcell Biochem 2014; 73: 137–52.

4 Yang B, Verkman AS. Urea transporter UT3 functions as an efficient water channel. Direct evidence for a common water/urea pathway. J Biol Chem 1998; 273: 9369–72.

5 Yang B, Verkman AS. Analysis of double knockout mice lacking aquaporin-1 and urea transporter UT-B. Evidence for UT-B-facilitated water transport in erythrocytes. J Biol Chem 2002; 277: 36782–6.

6 Zhao D, Sonawane ND, Levin MH, Yang B. Comparative transport efficiencies of urea analogues through urea transporter UT-B. Biochim Biophys Acta 2007; 1768: 1815–21.

7 Yang B. Transport characteristics of urea transporter-B. Subcell Biochem 2014; 73: 127–35.

8 Levin EJ, Zhou M. Structure of urea transporters. Subcell Biochem 2014; 73: 65–78.

9 Yang B, Bankir L, Gillespie A, Epstein CJ, Verkman AS. Urea-selective concentrating defect in transgenic mice lacking urea transporter UT-B.

J Biol Chem 2002; 277: 10633–7.

10 Bankir L, Chen K, Yang B. Lack of UT-B in vasa recta and red blood cells prevents urea-induced improvement of urinary concentrating ability. Am J Physiol Renal Physiol 2004; 286: F144–51.

11 Fenton RA, Chou CL, Stewart GS, Smith CP, Knepper MA. Urinary concentrating defect in mice with selective deletion of phloretin-sensitive urea transporters in the renal collecting duct. Proc Natl Acad Sci U S A 2004; 101: 7469–74.

12 Fenton RA, Flynn A, Shodeinde A, Smith CP, Schnermann J, Knepper MA. Renal phenotype of UT-A urea transporter knockout mice. J Am Soc Nephrol 2005; 16: 1583–92.

13 Verkman AS, Esteva-Font C, Cil O, Anderson MO, Li F, Li M, *et al*. Small-molecule inhibitors of urea transporters. Subcell Biochem 2014; 73: 165–77.

14 Li F, Lei T, Zhu J, Wang W, Sun Y, Chen J, *et al*. A novel small-molecule thienoquinolin urea transporter inhibitor acts as a potential diuretic. Kidney Int 2013; 83: 1076–86.

15 Ren H, Wang Y, Xing Y, Ran J, Liu M, Lei T, *et al*. Thienoquinolins exert diuresis by strongly inhibiting UT-A urea transporters. Am J Physiol Renal Physiol 2014; 307: F1363–72.

16 Liu Y, Esteva-Font C, Yao C, Phuan PW, Verkman AS, Anderson MO. 1,1-Difluoroethyl-substituted triazolothienopyrimidines as inhibitors of a human urea transport protein (UT-B): new analogs and binding model. Bioorg Med Chem Lett 2013; 23: 3338–41.

17 Anderson MO, Zhang J, Liu Y, Yao C, Phuan PW, Verkman AS. Nanomolar potency and metabolically stable inhibitors of kidney urea transporter UT-B. J Med Chem 2012; 55: 5942–50.

18 Lee S, Esteva-Font C, Phuan PW, Anderson MO, Verkman AS. Discovery, synthesis and structure-activity analysis of symmetrical 2,7-disubstituted fluorenones as urea transporter inhibitors. Medchemcomm 2015; 6: 1278–84.

19 Cil O, Esteva-Font C, Tas ST, Su T, Lee S, Anderson MO, *et al*. Salt-sparing diuretic action of a water-soluble urea analog inhibitor of urea transporters UT-A and UT-B in rats. Kidney Int 2015; 88: 311–20.

20 Esteva-Font C, Phuan PW, Lee S, Su T, Anderson MO, Verkman AS. Structure-activity analysis of thiourea analogs as inhibitors of UT-A and UT-B urea transporters. Biochim Biophys Acta 2015; 1848: 1075–80.

21 Levin EJ, Cao Y, Enkavi G, Quick M, Pan YP, Tajkhorshid E, *et al*. Structure and permeation mechanism of a mammalian urea transporter. Proc Natl Acad Sci U S A 2012; 109: 11194–9.

22 Magrane M, Consortium U. UniProt Knowledgebase: a hub of integrated protein data. Database (Oxford) 2011. doi:10.1093/database/bar009.

23 Song DD, Chen JX, Chen G, Li N, Li J, Fan J, *et al*. Parameterized BLOSUM matrices for protein alignment. IIEEE/ACM Trans Comput Biol Bioinform 2015; 12: 686–94.

24 Eisenberg D, Lüthy R, Bowie JU. VERIFY3D: assessment of protein models with three-dimensional profiles. Methods Enzymol 1997; 277: 396–404.

25 Lovell SC, Davis IW, Adrendall WB, de Bakker PIW, Word JM, Prisant MG, *et al*. Structure validation by C alpha geometry: phi, psi and Cbeta deviation. Proteins 2003; 50: 437–50.

26 Venkatachalam CM, Jiang X, Oldfield T, Waldman M. LigandFit: a novel method for the shape-directed rapid docking of ligands to protein active sites. J Mol Graph Model 2003; 21: 289–307.

27 Rogers D, Hopfinger AJ. Application of genetic function approximation to quantitative structure-activity relationships and quantitative structure-property relationships. J Chem Inf Comput Sci 1994; 34: 854–66.

28 Chang CC, Lin CJ. LIBSVM: a library for support vector machines. ACM Trans Intell Syst Technol 2011; 2: 27.

29 So SS, Karplus M. Evolutionary optimization in quantitative structure-activity relationship: an application of genetic neural networks. J Med Chem 1996; 39: 1521–30.

30 Stanton DT. QSAR and QSPR model interpretation using partial least squares (PLS) analysis. Curr Comput Aided Drug Des 2012; 8: 107–27.

31 Knepper MA, Miranda CA. Urea channel inhibitors: a new functional class of aquaretics. Kidney Int 2013; 83: 991–3.

32 Sands JM. Urea transporter inhibitors: en route to new diuretics. Chem Biol 2013; 20: 1201–2.

33 Esteva-Font C, Cil O, Phuan PW, Su T, Lee S, Anderson MO, *et al*. Diuresis and reduced urinary osmolality in rats produced by small-molecule UT-A-selective urea transport inhibitors. FASEB J 2014; 28: 3878–90.

34 Esteva-Font C, Anderson MO, Verkman AS. Urea transporter proteins as targets for small-molecule diuretics. Nat Rev Nephrol 2015; 11: 113–23.

35 Li M, Tou WI, Zhou H, Li F, Ren H, Chen CY, *et al*. Developing hypothetical inhibition mechanism of novel urea transporter B inhibitor. Sci Rep 2014; 4: 5775.